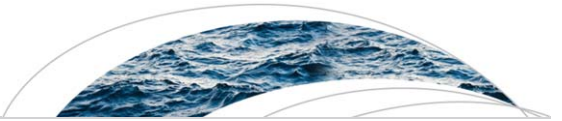
AGU PUBLICATIONS

Water Resources Research



RESEARCH ARTICLE
10.1002/2017WR021736

X-ray Microtomography of Intermittency in Multiphase Flow at Steady State Using a Differential Imaging Method

Ying Gao[1,2], Qingyang Lin[1], Branko Bijeljic[1,2], and Martin J. Blunt[1,2]

[1]Department of Earth Science and Engineering, Imperial College London, London, UK, [2]Qatar Carbonates and Carbon Storage Research Centre, Department of Earth Science and Engineering, Imperial College London, London, UK

Key Points:
- Differential imaging of fluid configurations during steady state brine/decane fractional flow coinjection at low and high capillary numbers
- At low *Ca* number the two phases flow in their own connected pathways as expected, while an intermittent phase was observed at high *Ca* number
- The relative permeability measured on our mm-scale core shows a good agreement with conventional experiments on cm-sized systems

Correspondence to:
Q. Lin,
q.lin11@imperial.ac.uk

Citation:
Gao, Y., Lin, Q., Bijeljic, B., & Blunt, M. J. (2017). X-ray microtomography of intermittency in multiphase flow at steady state using a differential imaging method. *Water Resources Research*, *53*. https://doi.org/10.1002/2017WR021736

Received 24 AUG 2017
Accepted 15 NOV 2017
Accepted article online 21 NOV 2017

© 2017. The Authors.
This is an open access article under the terms of the Creative Commons Attribution-NonCommercial-NoDerivs License, which permits use and distribution in any medium, provided the original work is properly cited, the use is non-commercial and no modifications or adaptations are made.

Abstract We imaged the steady state flow of brine and decane in Bentheimer sandstone. We devised an experimental method based on differential imaging to examine how flow rate impacts impact the pore-scale distribution of fluids during coinjection. This allows us to elucidate flow regimes (connected, or breakup of the nonwetting phase pathways) for a range of fractional flows at two capillary numbers, *Ca*, namely 3.0×10^{-7} and 7.5×10^{-6}. At the lower *Ca*, for a fixed fractional flow, the two phases appear to flow in connected unchanging subnetworks of the pore space, consistent with conventional theory. At the higher *Ca*, we observed that a significant fraction of the pore space contained sometimes oil and sometimes brine during the 1 h scan: this intermittent occupancy, which was interpreted as regions of the pore space that contained both fluid phases for some time, is necessary to explain the flow and dynamic connectivity of the oil phase; pathways of always oil-filled portions of the void space did not span the core. This phase was segmented from the differential image between the 30 wt % KI brine image and the scans taken at each fractional flow. Using the grey scale histogram distribution of the raw images, the oil proportion in the intermittent phase was calculated. The pressure drops at each fractional flow at low and high flow rates were measured by high-precision differential pressure sensors. The relative permeabilities and fractional flow obtained by our experiment at the mm-scale compare well with data from the literature on cm-scale samples.

1. Introduction

The understanding of multiphase flow in porous media is of vital importance in many subsurface applications, such as hydrocarbon recovery (Morrow & Buckley, 2011; Parker, 1989), and carbon dioxide storage (Andrew et al., 2013; Bachu, 2003). Fundamentally, multiphase flow is controlled by the interplay of viscous and capillary forces whose balance depends on the geometry and topology of the porous structure, wettability, and flow regime (Blunt, 2017). Different flow regimes are characterized by the ratio of viscous to capillary forces conventionally described by the capillary number, $Ca = \mu v/\sigma$, where in this paper μ is the mean viscosity of the flowing phases, υ is the total Darcy velocity, and σ is the interfacial tension. However, this does not represent a true ratio of forces during a displacement (Armstrong et al., 2014; Hilfer & Øren, 1996): later in the paper we will discuss the application of macroscopic measures of the balance of capillary and viscous forces. Channel flow and slug flow were first observed in flow cells made with a single layer of glass beads (Chatenever &Calhoun, 1952). Later studies on two-dimensional micromodels demonstrated that connected pathway flow and ganglion dynamics can occur side by side at the pore scale, and summarized different flow regimes as a function of capillary number, wetting phase relative permeability, viscosity ratio, and saturation (Avraam & Payatakes, 1996; Payatakes, 1982). Ganglion motion, namely the advection of discrete blobs of oil through the pore space, has been observed in micromodel experiments at capillary numbers greater than 10^{-3} (Tallakstad et al., 2009a, 2009b). In three-dimensional bead packs, the nonwetting phase can continually breakup into discrete ganglia, which are then advected through the pore space by the wetting fluid. The pore-scale flow regimes have been mapped in a "phase diagram" where the regimes of connected pathway flow and ganglion dynamics are characterized by fractional flow and capillary number (Armstrong et al., 2016; Datta et al., 2014a, 2014b). For sufficiently low flow rates, both fluids flow through unchanging, distinct, connected pathways for a given fractional flow; in contrast, at sufficiently large flow rates, the nonwetting fluid is broken up into discrete ganglia.

Recently, X-ray computed microtomography (micro-CT) has advanced to allow for the imaging of pore-scale displacement processes in geologically related studies, as well as for observations of dynamic pore-scale

phenomena in real rocks. Examples include dynamics of snap-off in multiphase flow, droplet fragmentation in carbonates, changes in pore structure during rock dissolution and oil shale pyrolysis (Al-Khulaifi et al., 2017; Andrew et al., 2015; Berg et al., 2014; Blunt et al., 2013; Menke et al., 2016; Pak et al., 2015; Saif et al., 2017; Singh et al., 2017; Wildenschild & Sheppard, 2013). In addition, differential X-ray imaging can characterize subresolution porosity in the complex pore structures of carbonate rocks (Lin et al., 2016) and visualize and quantify capillary drainage (Lin et al., 2017).

In the context of flow regimes, ganglion dynamics has also been observed using fast microtomography in a sintered glass bead pack (Rücker et al., 2015a). In consolidated sandstone, it has been shown that imbibition in porous rock is a two-stage process that involves a combination of connected pathway flow and ganglion dynamics (Berg et al., 2016; Rücker et al., 2015b). Reynolds et al. (2017) studied the flow of nitrogen and brine flowing at the same rate in Bentheimer sandstone: they demonstrated a dynamic connectivity of the phases where pathways of the nitrogen periodically connect and disconnect. This is a different type of behavior, where ganglia of the nonwetting phase do not advect through the pore space, but instead local rearrangements of the pore occupancy allow flow sporadically, analogous to the stop-and-start of cars on roads controlled by traffic lights. Connected paths of the nonwetting phase are only seen at capillary numbers around 10^{-7} or lower, which is two orders of magnitude lower than the onset of ganglion dynamics observed in bead packs by Datta et al. (2014a).

There are thus two possible scenarios where a nonwetting phase is mobile even though not permanently connected between inlet and outlet. First, because of viscous mobilization by the externally applied flow field of the nonwetting phase that pushes the nonwetting phase through the pore space, where the viscous pressure drop over a ganglion exceeds the capillary entry pressure of the next pore throat (see, for instance, Armstrong et al., 2014). In this work, we study steady state experiments, where the capillary pressure remains constant along the core. In this case, there is no driving force for viscous mobilization, regardless of flow rate. Second, an intrinsic mobilization triggered by a sequence of breakup and coalescence caused by local pressure fluctuations (Rücker et al., 2015b) referred to as dynamic connectivity by Reynolds et al. (2017). This behavior can be captured using numerical simulation of multiphase flow through pore-space images. For instance, Armstrong et al. (2016, 2017) studied the flux contribution of disconnected phases as a function of fractional flow and capillary number. They demonstrated that at low nonwetting phase saturation, the dominant contribution to flow of the nonwetting phase was from disconnected phases over a wide range of capillary number.

Most of the work described above used fast micro-CT at synchrotrons where images could be acquired in less than a minute: laboratory-based instruments provide longer access, but have greater scan times. In this paper, we will study the behavior over a range of fractional flows and combine laboratory imaging with sensitive pressure measurements which will allow the simultaneous estimation of relative permeability at the mm scale. It is not possible to identify rapid changes in pore occupancy from comparing images, since these will be taken an hour or more apart. Instead we will devise a differential X-ray imaging method that can identify intermittent pore occupancy during simultaneous injection of wetting and nonwetting phases in the pore space of Bentheimer sandstone. We will quantify the flow behavior at two capillary numbers $Ca = 3.0 \times 10^{-7}$ and $Ca = 7.5 \times 10^{-6}$ representing two flow regimes over a range of fractional flows (0, 0.15, 0.3, 0.5, 0.7, 0.85, and 1). We focus on two particular aspects: (i) to discriminate and quantify the intermittent phase and connectivity and (ii) to measure relative permeability and compare our results with experiments on cm-scale samples.

2. Experimental Methodology

2.1. Rock Samples and Fluids Properties

The rock sample we used in this study was Bentheimer sandstone, which contains 95% quartz, 4% feldspar, and approximately 1% fine clay (analysis conducted at the Natural History Museum, London, UK). The samples were drilled into cylindrical cores 4.99 ± 0.01 mm in diameter and approximately 30 mm in length. The absolute permeability measured at the same experimental condition is $2.045(\pm 0.056) \times 10^{-12}$ m^2. The porosity measured based on our image is $21.95 \pm 0.52\%$.

The brine solution was made from deionized water with a prescribed amount of Potassium Iodide (KI). KI was used as an ionic salt as it has a high atomic weight causing a large X-ray attenuation coefficient, allowing it to be used as a contrast agent. A solution of 30 wt % KI (2.58 mol/kg) in deionized water was used as

the wetting phase, which provided an effective contrast between brine, oil, and rock phases (Lin et al., 2016). Decane was used as the nonwetting phase.

The interfacial tension (IFT) between brine and decane was measured to be 47.05 ± 1.56 mN/m at ambient conditions measured by a Ramé-Hart apparatus (590 F4 series) using the pendant drop method (Andreas et al., 1938; Stauffer, 1965). The density of brine was measured to be 1,263 ± 2 kg/m^3 at ambient conditions by measuring the mass of a 1 mL drop of liquid. The accuracy of the mass balance is 0.001 g, and that of the volume pipette is 0.001 mL. The density of decane is 730 kg/m^3 (n-decane, Acros Organics).

2.2. Experimental Methodology

The flow loop of the apparatus is shown in Figure 1a. The experiments were conducted in a Hassler type flow cell made of carbon fiber that is X-ray transparent. Two samples were assembled in series, the bottom one was used as "diffuser" to mix the oil and water together, which helps ensure that two fluids flow into the second core simultaneously (Figure 1b). The length of the two samples was 29.1 ± 0.01 and 30.9 ± 0.01 mm. The total length was therefore about 60 mm. These two cores were then placed into a fluoropolymer elastomer (Viton) sleeve, which was attached to metal fittings (end piece) connecting the core to the pore-fluid flow lines.

The flow regime depends on the fractional flow and the capillary number. In this work, the low total flow rate was 0.02 mL/min and the high total flow rate was 0.5 mL/min. The viscosity of brine is 0.822 ± 0.013 mPa s, and that of decane is 0.838 mPa s (provided by PubChem, open chemistry database). The capillary numbers used in this work were calculated by the total flow rates of brine and decane, and the average viscosity of both fluids, because of their similar viscosity. The fractional flow is given by the injection rate ratio of each fluid to the total fluid rate: the capillary number for the low and high flow rate experiments are 3.0×10^{-7} and 7.5×10^{-6}, respectively. For each experiment, we kept the total flow rate fixed as we varied the fractional flow.

We can also define a macroscopic capillary number (Hilfer & Øren, 1996):

$$Ca^{macro} = \frac{vL\mu_w}{KP_c} \tag{1}$$

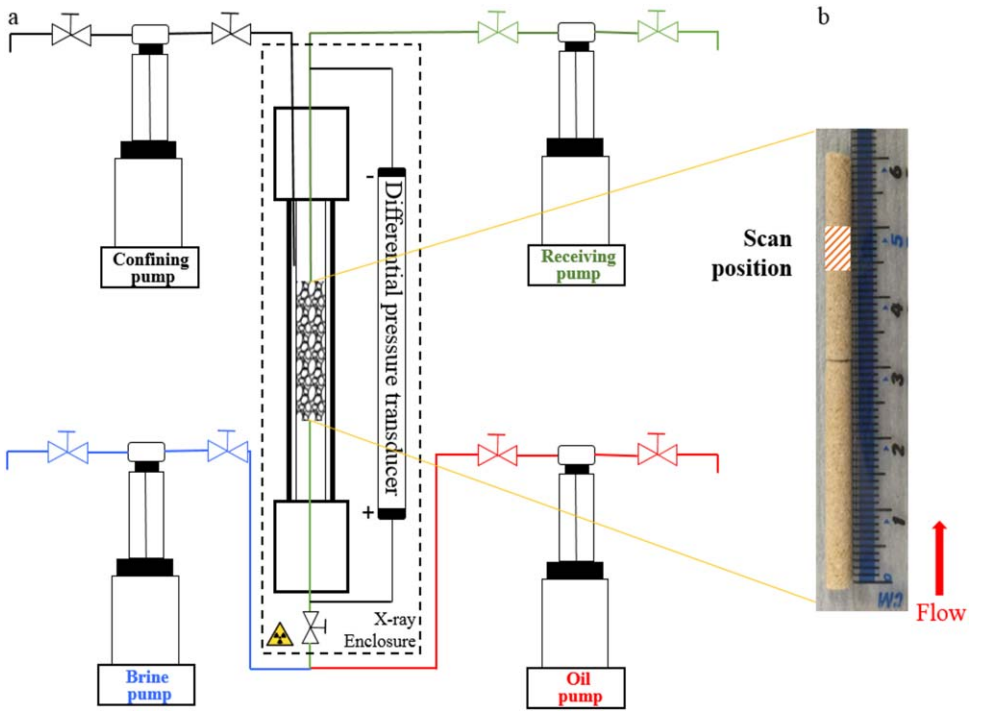


Figure 1. Experimental apparatus. (a) The pumps used to control the flow and the siting of the flow cell within the micro-CT enclosure. (b) Detail of the core arrangement. The bottom core acted as a "diffuser" to ensure there is no slug flow. Tomographic scans were taken near the top of the downstream core, as shown. The "+" is linked to the tubing at the inlet of the core holder and the "−" linked to the tubing of the outlet of core holder.

where L represents a cluster length, K is the permeability, and P_c is a capillary entry pressure. Using our measured values, where we assume that the cluster length is the core size (30 mm; consistent with, in most cases, the nonwetting phase being connected across the system, see later), and a typical capillary pressure of 4 kPa (Blunt, 2017), we have values of 5.0×10^{-2} and 1.3 for the low and high rate experiments, respectively. For the lower flow rate, viscous forces are still small at the core scale, while for the higher rate viscous and capillary forces are approximately equal. Hence, we study two distinct large-scale flow regimes: one where capillary forces are always dominant and one where viscous forces are significant at the core scale.

The experiments were conducted using the following procedures:

1. A confining pressure of 2 MPa was applied and maintained within the cell to compress the Viton sleeve around the core sample to avoid any fluid bypass.
2. A dry (air) scan of 1 h was taken at room temperature.
3. The core was flooded with gaseous CO_2 for 30 min to remove air.
4. Brine was injected and the differential pressure transducer (PD-33X, Keller) was linked along the tubing. The "+" linked to the tubing at the inlet of the core holder and the "−" linked to the tubing of the outlet of core holder. It was checked that there was no air in the tubing linking between the main flow line

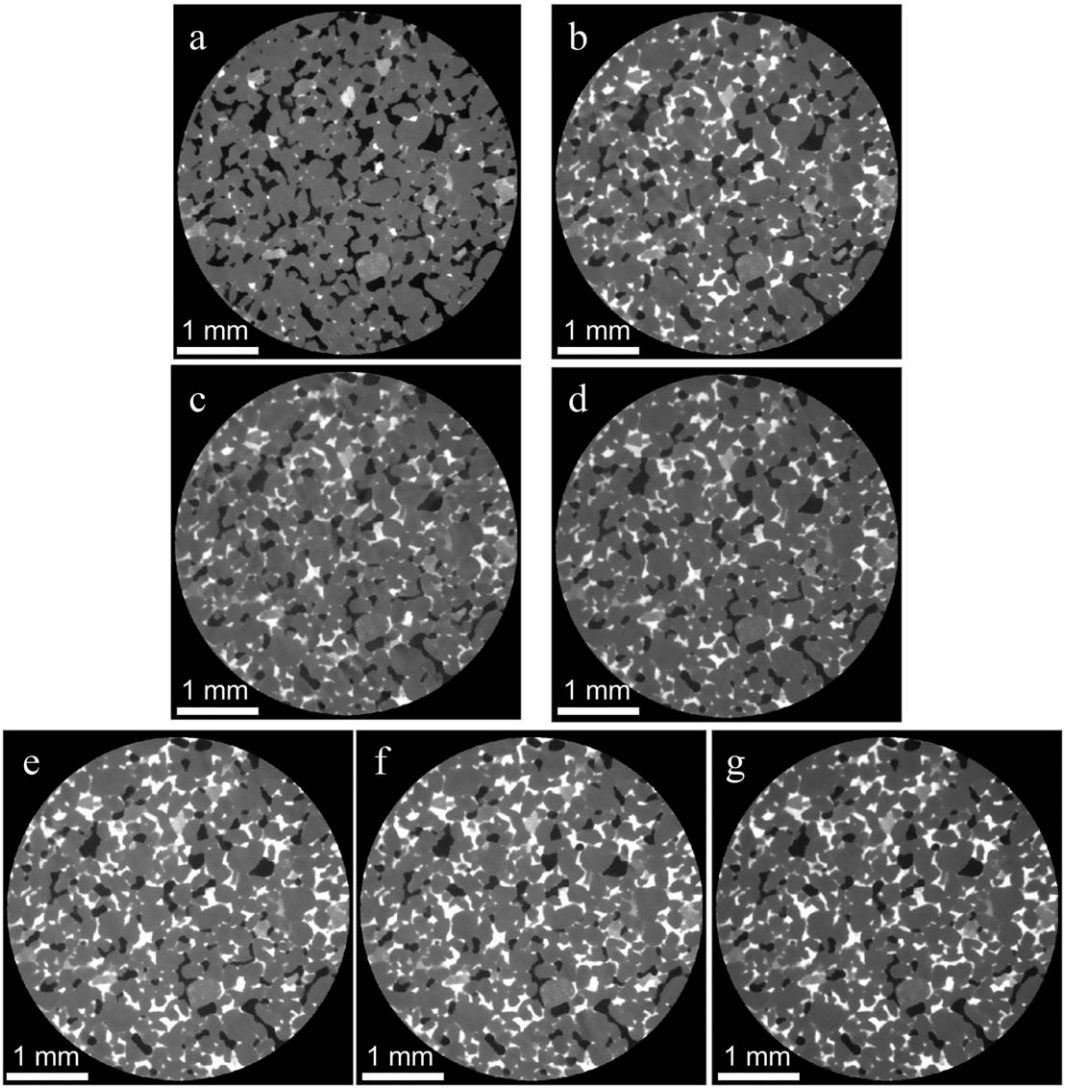


Figure 2. Two-dimensional cross sections of three-dimensional micro-CT images of the middle slice at different fractional flows when Ca is 3.0×10^{-7}. From left to right and from top to bottom, the fraction flow is 0, 0.15, 0.3, 0.5, 0.7, 0.85, and 1. The grey is grain, the black is oil, and the white is brine.

and transducers. The tubing remained full of water during the experiment and so it is assumed that the transducer measures the pressure difference in the water phase. The range of the differential pressure transducer is 300 kPa, and the accuracy is 0.1% over the whole range.

5. Then brine was injected from the brine pump at a flow rate (1 mL/min) for more than 5 h through the core sample to ensure it is fully saturated with brine.
6. After 100% brine saturation was achieved a brine saturated scan for 1 h was taken: the scan confirmed full saturation.
7. The first step was primary drainage and only oil was injected into the core to obtain the initial water saturation. For the low *Ca* experiment (see step 11 for the high *Ca* experiment) the two pumps were 100DX High Pressure Syringe Pump (Teledyne Isco Syringe Pumps). The flow range of the pump was from 0.01 μL/min to 50 mL/min, and the accuracy was ±0.3% of setpoint.
8. Wait until the flow reached steady state. It took about 20 h to reach the steady state at low *Ca* to see stable conditions, which were identified by observing a stable and constant pressure drop, see section 3.5. Then a scan was taken over a period of 1 h without stopping the fluid injection.
9. Steps 6 and 7 were repeated at water fractional flows of 0.15, 0.3, 0.5, 0.7, 0.85, and 1 by changing the flow rates of the oil and brine pumps while keeping the total volumetric flow rate constant. The oil flow

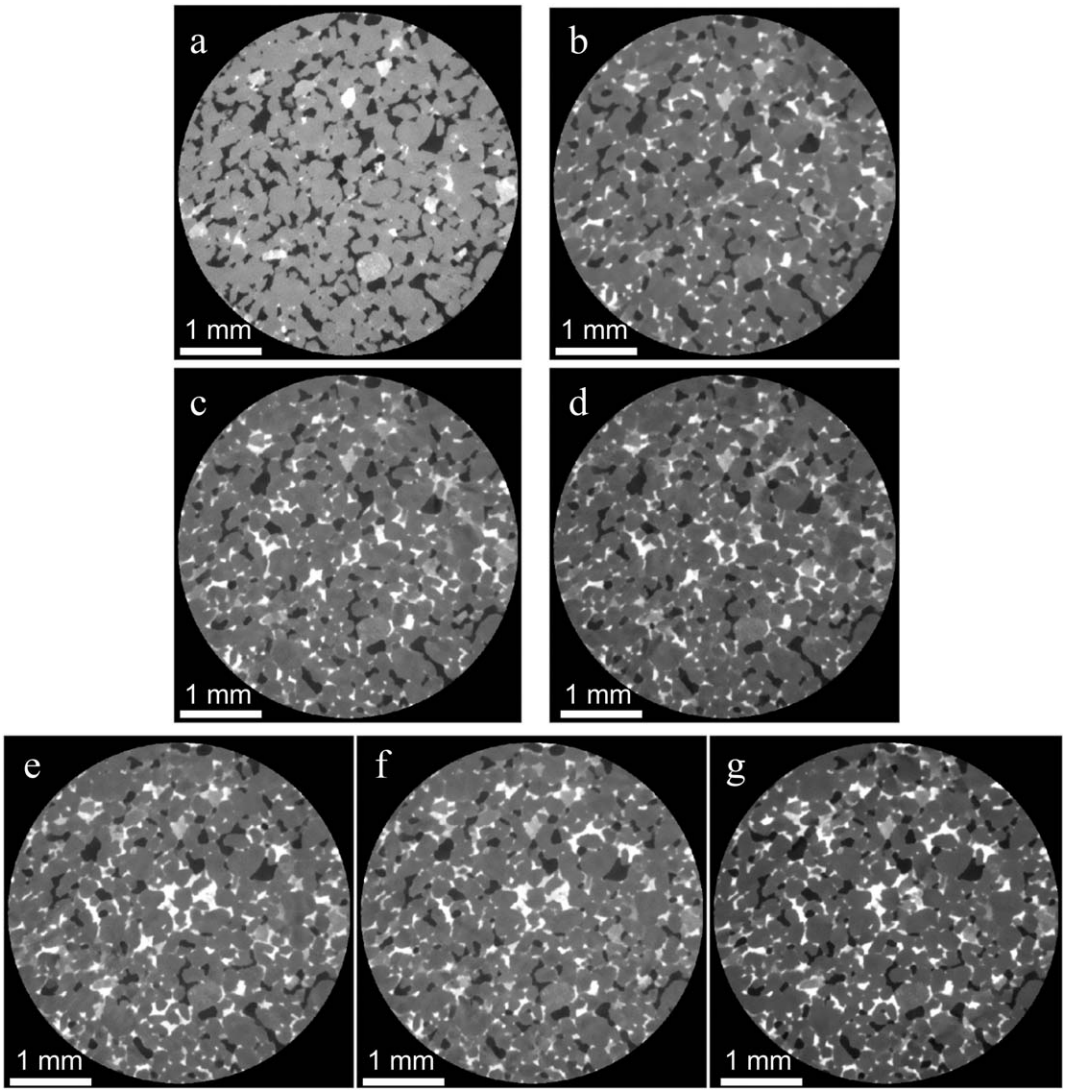


Figure 3. Two-dimensional cross sections of three-dimensional micro-CT images of the middle slice at different fractional flows when *Ca* is 7.5×10^{-6}. From left to right and from top to bottom, the fractional flow is 0, 0.15, 0.3, 0.5, 0.7, 0.85, and 1. The grey includes grain and intermittent oil, the black is stable oil, and the white is brine.

rate decreased from 0.02 to 0 mL/min and the brine flow rate increased from 0 to 0.02 mL/min. The experiments, therefore, represent an imbibition displacement. The pressure difference at each fractional flow was recorded.

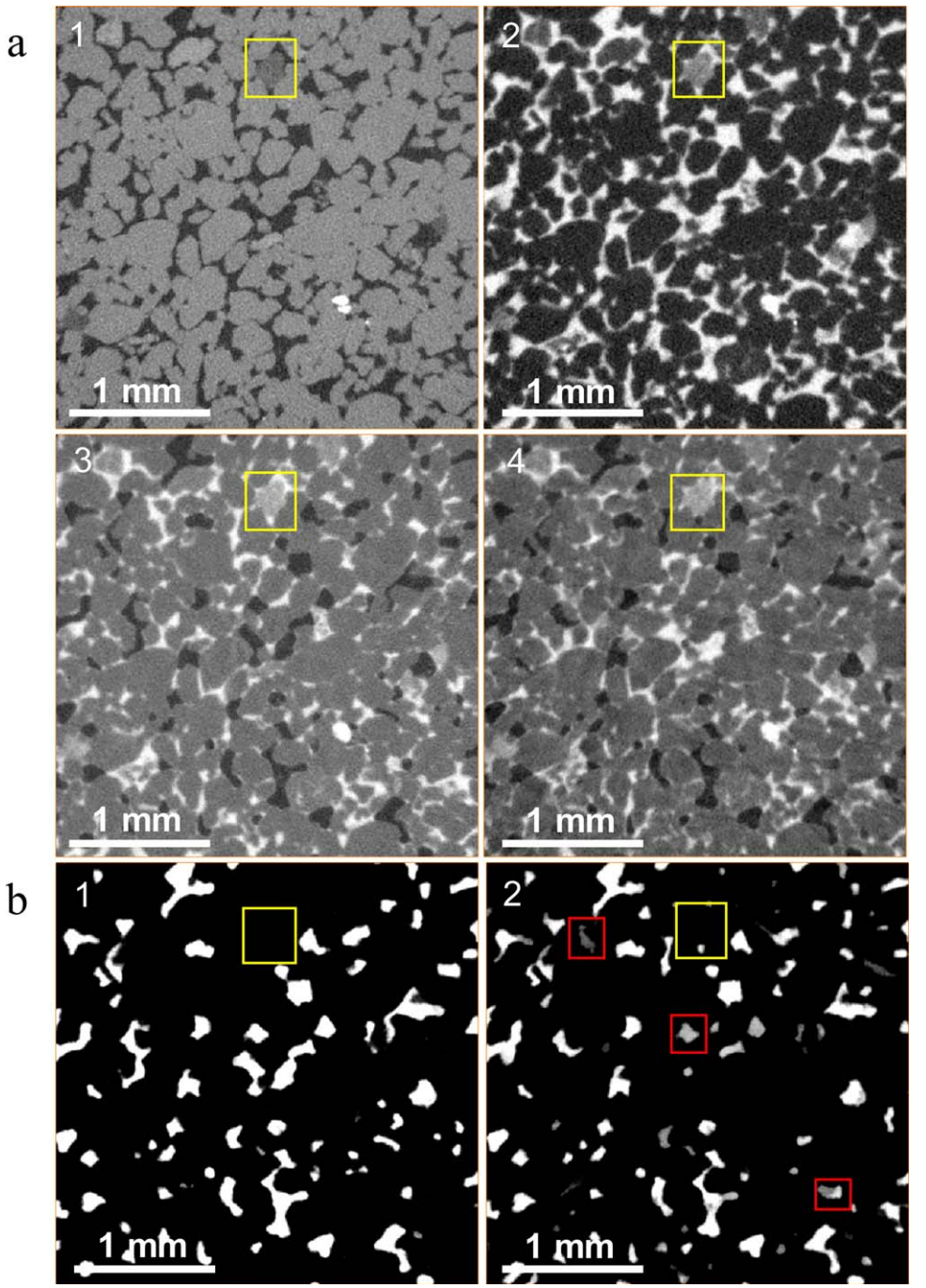


Figure 4. (a) Two-dimensional cross sections of three-dimensional micro-CT images. (1) An example of dry scan. (2) Sample saturated with brine. (3) Image after coinjection of oil and brine at the lower *Ca* when f_w was 0.5. (4) Image after coinjection of oil and brine at the higher *Ca* when f_w was 0.5. The yellow boxes indicate regions containing micropores. (b) The difference in grey scale values between the KI saturated scans and the multiphase scan at low *Ca* (1) and high *Ca* (2) at steady state. The two-dimensional slices show that three phases including solid grain phase and unchanged brine (dark), redistributed oil (intermediate grey), and oil phase (bright) can be distinguished. The yellow boxes (see Figure 4a) show that the micropores are only occupied by brine. The red boxes show the presence of grey in the differential image indicating intermittent pore occupancy.

10. The core was cleaned by injecting more than 1,000 mL deionized water at 1 mL/min for more than 5 h and put in an oven at 80°C for 12 h to dry it.
11. The flow rate of the second set of experiments was 0.5 mL/min ($Ca = 7.5 \times 10^{-6}$). Steps 2–10 were repeated. It took about 10–15 h to reach steady state in this case. For the higher *Ca* experiment, the two pumps were 1,000 D High Pressure Syringe Pump (Teledyne Isco Syringe Pumps). The flow range of the pump was from 0.1 to 408 mL/min, and the accuracy was ±0.5% of setpoint. The reason we chose a larger volume pump was that the volume of the 100 D pump was too small (102.93 mL) to flood constantly for 15 h.
12. By repeating the same steps from step 7 to step 9, the pressure difference during flow in only the tubing between the inlet and outlet at each fractional flow at low and high *Ca* was measured after removing the cores. For the lower *Ca*, the pressure drop along the tubing was from 0.1 to 0.9 kPa. For the higher *Ca*, it was from 2 to 21 kPa. The pressure difference was the smallest when f_w was 0, and was the largest when f_w was 0.5 and 0.75.
13. The pressure drops in the cores were calculated by subtracting the pressure drops along the tubing measured at step 12 from the total pressure drops measured at step 9.

3. Results and Discussion

We devise a differential imaging method to first examine impact of subresolution pores in coinjection (section 3.3) and then to quantify the intermittent phase during a coinjection experiment (sections 3.4.1 and 3.4.2). Further, the grey scale distribution of the raw multiphase images is used to calculate the oil saturation (section 3.4.3). Finally, the relative permeabilities are calculated based on the pressure drop measured between the inlet and outlet (section 3.5).

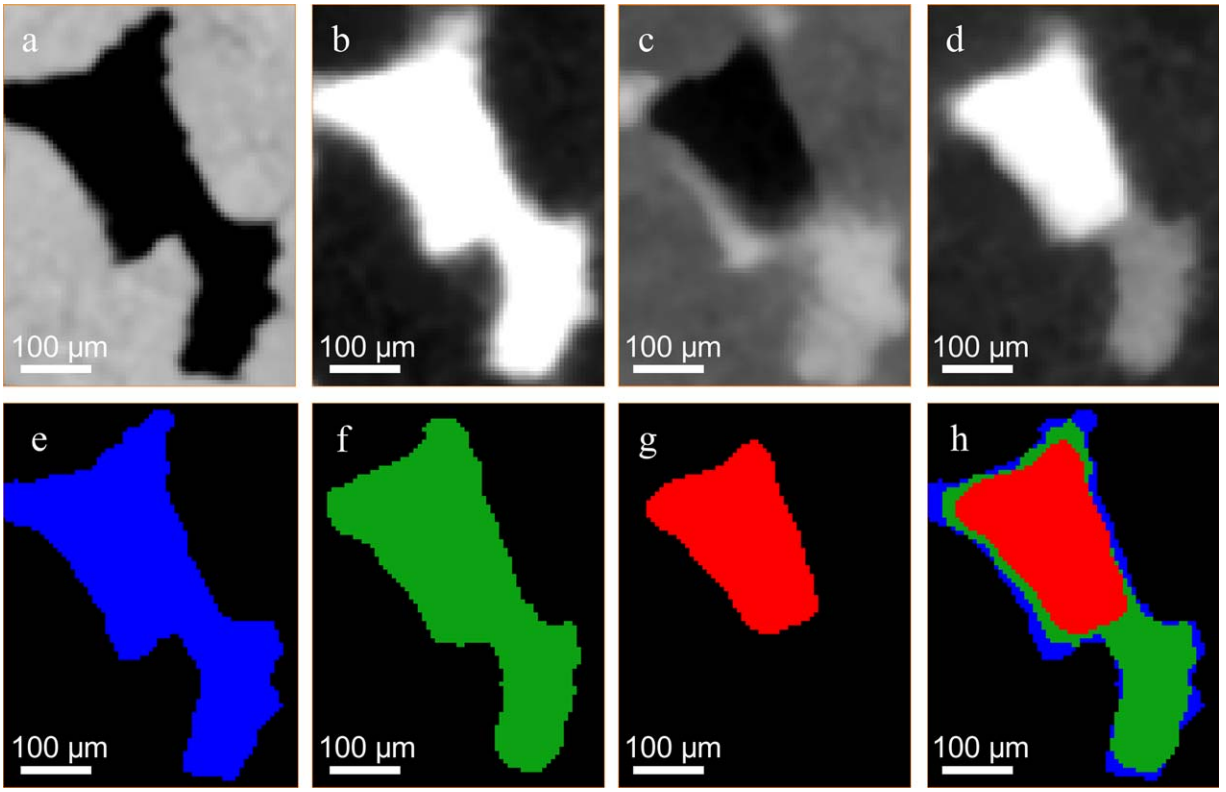


Figure 5. Illustration of the steps in segmentation: (a) An example pore of the dry scan. (b) The same pore imaged when fully brine saturated. (c) The same pore imaged during steady state multiphase flow at a fixed fractional flow. (d) Differential image between Figures 5b and 5c after normalization. (e) The pore segmentation. (f) Segmented intermittent and oil phase in the pore space. (g) Segmented oil phase in the pore. (h) Segmented oil, brine, and intermittent phase. The red is oil, the blue is brine, and the green is the intermittent phase.

3.1. Grey Scale Images

The rock and fluids were imaged using a Zeiss XRM-500 X-ray microscope at a voxel size of 6 μm. The images used for analysis are cropped cylindrical sections to avoid artifacts at the boundaries of the core. The image size was 710 × 710 × 800 voxels, or 4.26 mm diameter and length 4.8 mm, which represents a bulk volume of 68 mm^3, or approximately three fifths of the total size of the imaged sample. After reconstruction, all the images were registered to the dry scan image to have the same orientation using normalized mutual information, and resampled using the Lanczos algorithm (Burger & Burge, 2016). Figure 2 and 3 show two-dimensional cross sections of three-dimensional micro-CT images at low and high *Ca*, respectively, over a range of fractional flows.

3.2. Differential Images and Dynamic Connectivity at Different *Ca*

Even though all the images were taken at the same scan conditions, the grey scale value of each voxel was different because of varying fluid proportions and corresponding X-ray attenuation. Image normalization is a method to match the frequency of the grey scale histogram of the multiphase image with that of the

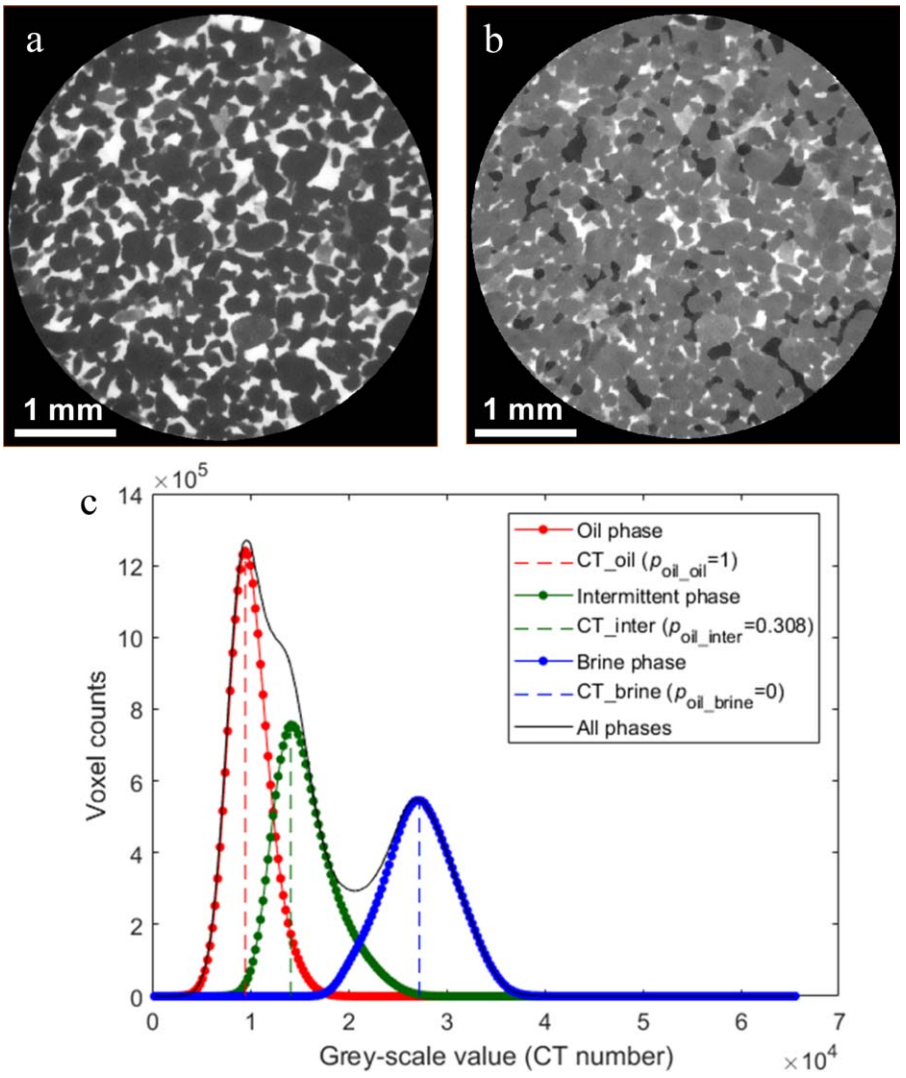


Figure 6. (a) The middle slice of the brine-saturated image. (b) The middle slice of multiphase image when f_w is 0.5 at the higher *Ca*. (c) The histograms for the three phases in the multiphase scan. The red dashed line indicates the average grey scale of the oil phase, the blue dashed line indicates the average grey scale of the brine phase, and the green dashed line shows the average grey scale of the intermittent phase. The proportion of oil in the intermittent phase is 0.308. The contribution to the oil saturation in the intermittent phase is calculated using equation (3). In this case, the value is 0.101.

brine images, which helps to distinguish the different phases. It can avoid the impact from image artifacts and aids more accurate segmentation.

Using 30 wt % KI brine helps to maximize the phase contrast between the oil and water phases. The main requirement of differential imaging method is to enhance the phase contrast. 30 wt % KI has been used to visualize and quantify the subresolution porosity in carbonates (Lin et al., 2016). In this study, to quantify fluid intermittency, the brine phase is also doped with 30 wt % KI. In principle, either phase can be doped in order to enhance the phase contrast, e.g., dope the oil phase with iododecane. The reason for doping the wetting phase is because it can fully saturate the core and we can check that initially there is no air present in the brine phase at the start of the experiment. The image contrast between pure deionized water and air under X-ray is not good, especially in small pores. The use of differential imaging between the brine saturated scan and the multiphase scan identifies clearly changes in fluid occupancy.

The difference image between the KI saturated scan and the multiphase scan is defined as:

$$\mathrm{CT}\ (\mathrm{differential}) = \mathrm{CT}\ (\mathrm{brine\ \ scan}) - \mathrm{CT}\ (\mathrm{multiphase\ \ scan}) + \mathrm{CT0} \tag{2}$$

where CT is the CT number of each voxel and CT0 is a constant value to avoid negative grey scale values.

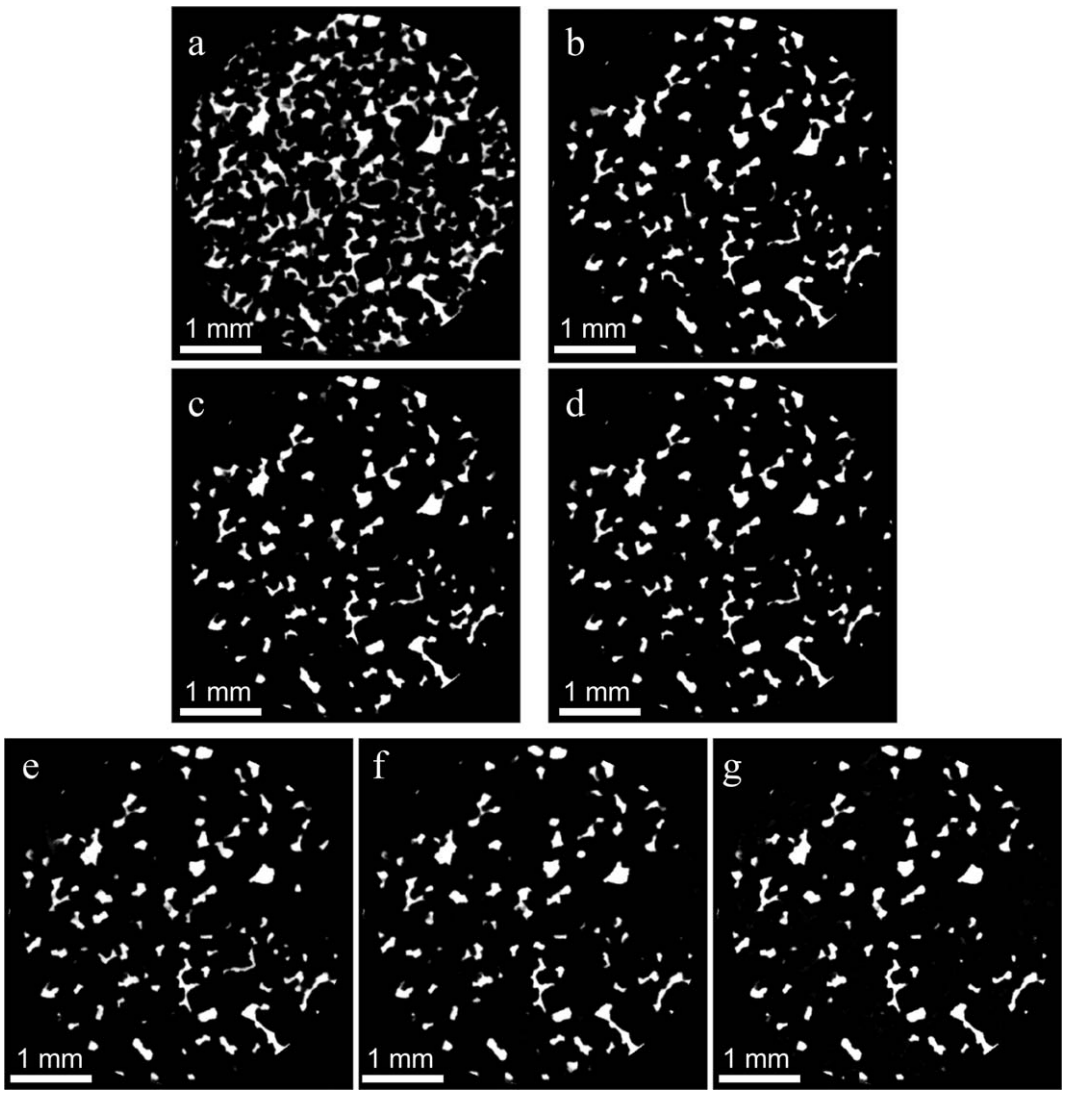


Figure 7. Two-dimensional cross sections of three-dimensional differential images of the middle slice at different fractional flows when *Ca* is 3.0×10^{-7}. From left to right and from top to bottom, the fractional flow is 0, 0.15, 0.3, 0.5, 0.7, 0.85, and 1. Black includes grains and unchanged brine, and white is oil.

Figure 4a shows the dry, brine, and multiphase image when the water volumetric fractional flow, f_w, is 0.5 at the low and high *Ca*. Figure 4b demonstrates the differential image at different conditions.

At the lower capillary number, there is only black and white in the differential image, thus the nonwetting phase is transported in distinct connected pathways which do not appear to change during the hour-long scan time. However, at high capillary number, intermediate grey values are seen in the differential image (indicated by red boxes in Figure 4b2), which suggests that the nonwetting phase is only present for some of the time during the scan at steady state—this represents the observation of intermittent behavior. Locally the pore-scale configuration of fluid rearranges.

3.3. The Impact of Subresolution Pores During Coinjection

The differential imaging method is first used to evaluate the saturation in subresolution pores. Based on the dry scan and fully brine-saturated image shown in Figure 4a1 and 4a2, some subresolution pores exist in Bentheimer: this has also been observed even in bead packs (Georgiadis et al., 2013). As Figure 4b shows, the grey regions, indicated by the yellow boxes, are dark in the differential image (Figure 4a) which confirms that oil does not enter these regions. The capillary entry pressure is insufficient for the oil phase to displace brine from these small pores.

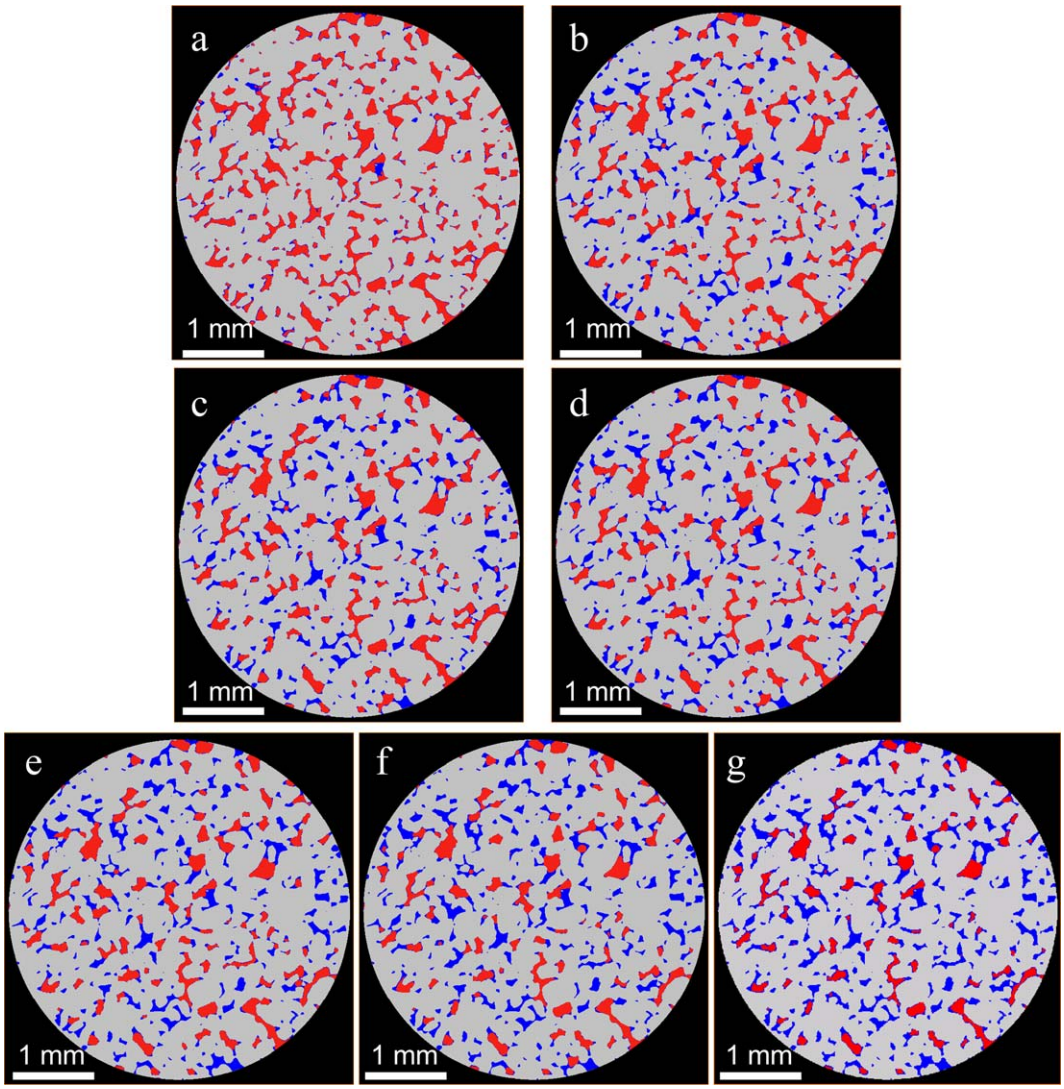


Figure 8. Two-dimensional cross sections of three-dimensional segmented images of the middle slice at different fractional flows when *Ca* is 3.0×10^{-7}. From left to right and from top to bottom, the fractional flow is 0, 0.15, 0.3, 0.5, 0.7, 0.85, and 1. The grey is grain, the red is oil, and the blue is brine.

3.4. Quantification of Phase Saturation and Occupancy

3.4.1. Image Processing and Segmentation-Based Differential Imaging

The differential images were preprocessed by filtering with a nonlocal means edge preserving filter to reduce the image noise (Buades et al., 2005, 2008). This is a linear filter where the grey scale of a certain voxel is replaced by the average of the grey scales of other voxels. In contrast to the standard mean filter, each voxel within the search area is assigned a weight proportional to an index measuring the similarity of the weighted voxel to the voxel being replaced by the filter. Each voxel is essentially averaged with other voxels similar to it, including interface voxels, which means that edges are preserved. Then the filtered differential images were processed with intensity-based thresholding to identify brine, oil, and redistributed (intermittent) phases, as described below—for more details see Lin et al. (2016).

Segmentation of the intermittent phase follows the procedure shown in Figure 5. The pore space was segmented based on the differential image between the dry scan and the brine scan, shown in Figure 5e. Intermittent and oil phase (Figure 5f) was segmented based on Figure 5d. Stable oil (Figure 5g) was identified based on the differential image. The intermittent phase was segmented by obtaining the difference between Figures 5f and 5g.

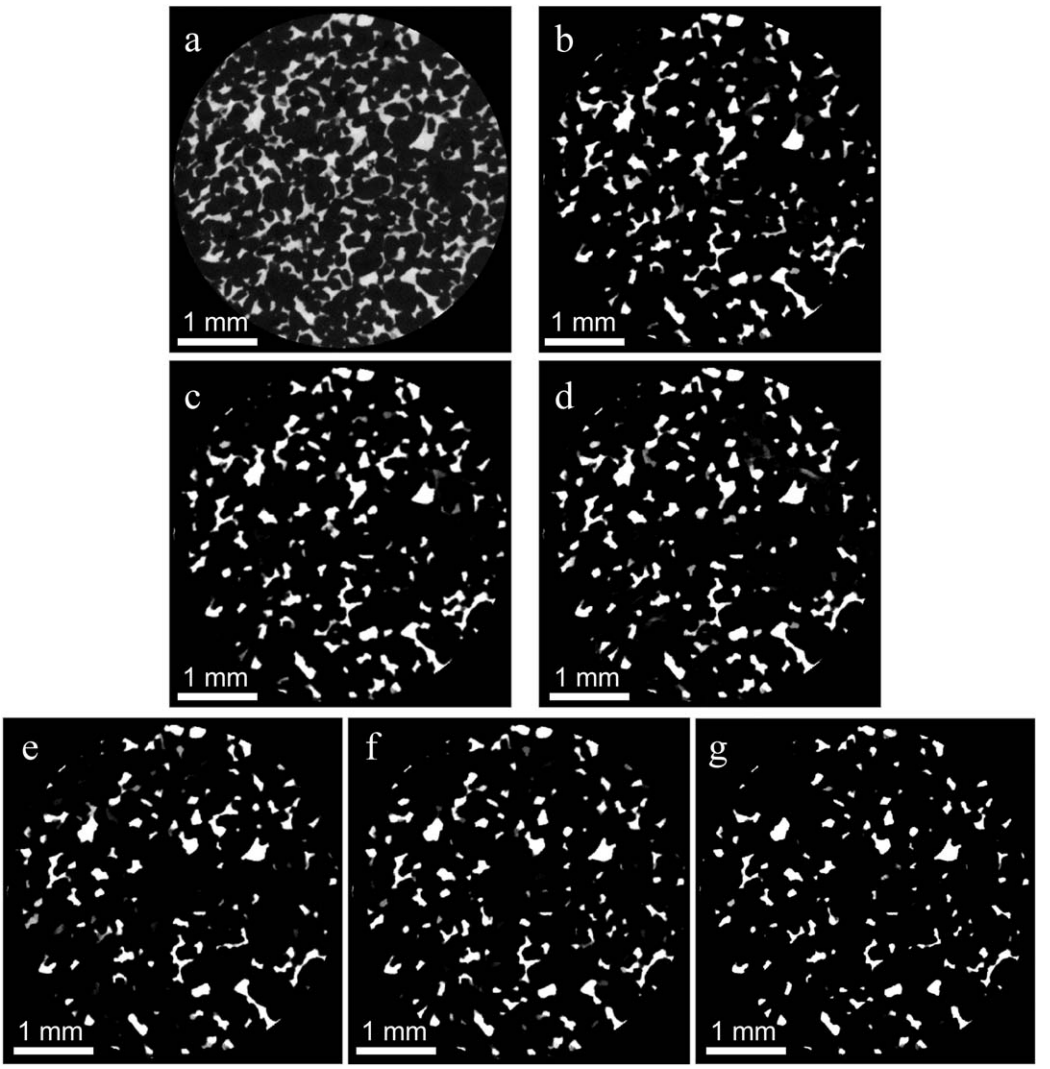


Figure 9. Two-dimensional cross sections of three-dimensional differential images of the middle slice at different fractional flows when *Ca* is 7.5×10^{-6}. From left to right and from top to bottom, the fractional flow is 0, 0.15, 0.3, 0.5, 0.7, 0.85, and 1. Black includes grains and unchanged brine, white is oil, and grey is the intermittent phase.

3.4.2. Quantification of the Intermittent Phase Saturation

At the lower *Ca*, the oil saturation was obtained from the differential images directly as no intermittent phase was identified. The water saturation was calculated based on the total porosity of the whole sample and the fraction of the pore space occupied by oil. The total porosity, ϕ, was 21.95 $\pm$ 0.52%, calculated based on the differential image between the fully brine-saturated image and the dry scan, including subresolution porosity. However, the oil saturation was not so straightforward to quantify at the higher *Ca*, since it was necessary to estimate the time-averaged oil saturation in the intermittent regions.

Using the segmented label images as reference, the histograms of CT number for all grey scale voxels in the multiphase images can be plotted for each phase, Figure 7: we require these histograms to quantify the intermittent phase. The grey scale values where the peak values are located for each phase in the histogram are denoted as *CT_oil* for the stable oil phase, *CT_inter* for the intermittent phase, and *CT_brine* for the stable brine phase. These values represent the most likely CT numbers for each phase. In the multiphase images, the contribution to the oil saturation in the intermittent phase is estimated as:

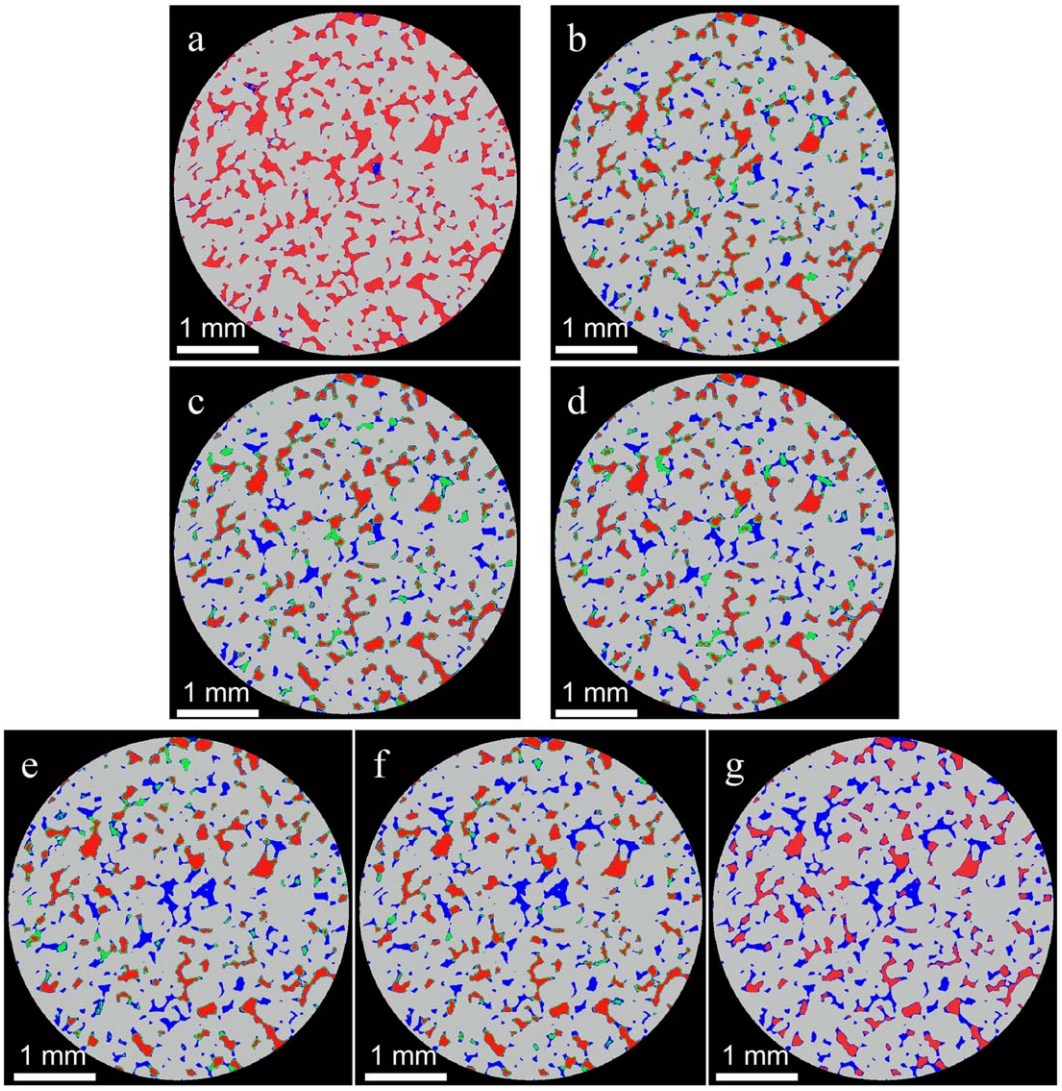


Figure 10. Two-dimensional cross sections of three-dimensional segmented images of the middle slice at different fractional flows when *Ca* is 7.5×10^{-6}. From left to right and from top to bottom, the fractional flow is 0, 0.15, 0.3, 0.5, 0.7, 0.85, and 1. The grey is grains, the red is oil, the blue is brine, and the green is rearranged or intermittent oil phase.

Table 1
Percentages of the Stable Oil, Stable Water and Intermittent Phases, as Well as the Water Saturation

	$Ca = 3.0 \times 10^{-7}$, $Ca^{macro} = 0.05$		$Ca = 7.5 \times 10^{-6}$, $Ca^{macro} = 1.3$					
f_w	S_w	Percentage of oil connected from inlet to outlet	Percentage of stable oil	Percentage of intermittent phase	Percentage of stable water	S_w	Percentage of oil and intermittent phase combined connected from the inlet to outlet	Percentage of stable oil connected from inlet to outlet
0	0.252	99.5	0.855	0	0.145	0.145	99.6	99.6
0.15	0.463	93.0	0.427	0.149	0.424	0.528	88.9	62.1
0.3	0.491	86.9	0.361	0.297	0.342	0.552	83.5	0
0.5	0.517	84.0	0.339	0.328	0.333	0.560	67.3	0
0.7	0.536	81.6	0.310	0.320	0.370	0.592	22.3	0
0.85	0.589	62.7	0.291	0.292	0.417	0.622	0	0
1	0.642	0	0.337	0	0.663	0.663	0	0

Note. Also shown is the fraction of the oil that connects from inlet to outlet, hence allowing flow and displacement, considering just the stable oil phase, and for the stable oil and intermittent phase combined.

$$S_{oil_inter} = S_{inter} p_{oil} = S_{inter} \frac{CT_inter - CT_oil}{CT_brine - CT_oil} \quad (3)$$

where S_{oil_inter} is the contribution to the oil saturation in the intermittent phase, S_{inter} is the fraction of the intermittent phase to the total pore volume, *CT_oil* is the average grey scale of the stable oil phase, *CT_inter* is the average grey scale of the intermittent phase, and *CT_brine* is the average grey scale of the brine phase. p_{oil} is the proportion of oil in the intermittent phase.

As shown in Figure 6, for the case when f_w is 0.5, the proportion of the oil in the intermittent phase, p_{oil}, is 0.308, while the fraction of the pore volume occupied by the intermittent phase, S_{inter}, is 0.328. Hence, the contribution to the oil saturation in the intermittent phase S_{oil_inter} is 0.101. The stable oil saturation is 0.339 and so the total oil saturation is 0.440.

3.4.3. Saturation at Low and High *Ca*

Figure 7 shows the differential images at different fractional flows for the low *Ca* experiment: white indicates oil. In these experiments, the two fluid phases appear to have a temporally fixed pore-scale occupancy: this

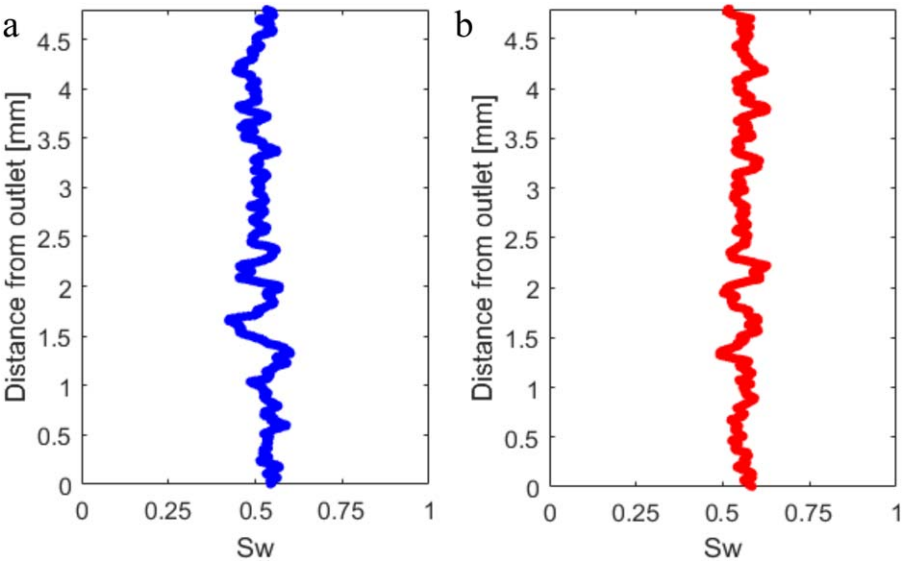


Figure 11. Sliced-averaged brine saturation distribution along the sample. (a) Brine saturation distribution when f_w is 0.5 at low *Ca*. The mean S_w is 0.517. (b) Brine saturation distribution when f_w is 0.5 at high *Ca*. The mean S_w is 0.560. The saturation profiles at all the other fractional flows also show that the saturation is constant along the sample.

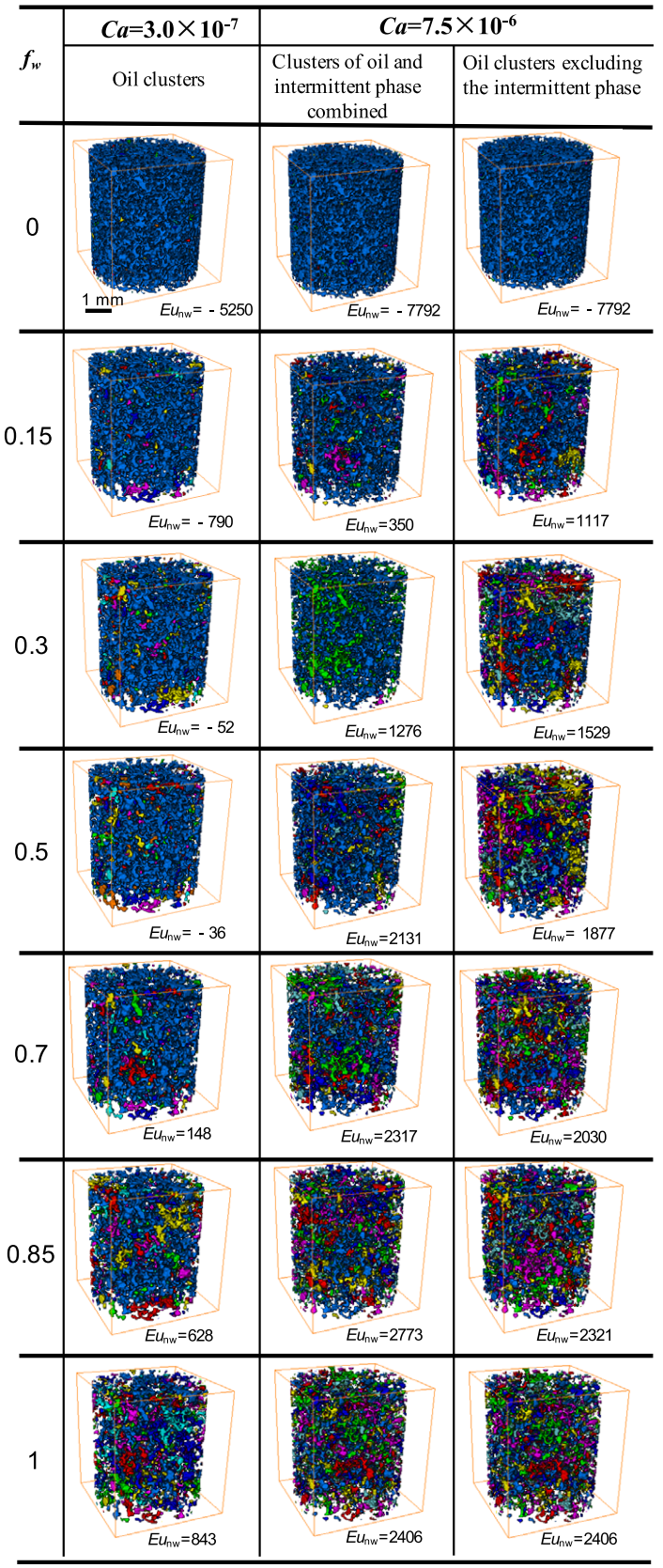


Figure 12. (continued)

occupancy changes—there is less oil—only when the water fractional flow increases. Figure 8 shows the same images segmented into brine, oil and rock phases. Figure 9 shows the difference images for the high *Ca* experiment. Here an intermediate grey phase is apparent, indicating that the occupancy in some of the pore space is intermittent. During the hour-long time of the scan it appears that some of the time these regions were oil-filled and at other times brine-filled. Figure 10 shows these images segmented into brine, oil, rock, and intermittent phases.

The average saturation of all phases, taken over the entire volume analyzed, can be found, and the values are listed in Table 1. Overall the slice-averaged saturation is approximately constant along the imaged portion of the core, as shown in Figure 11.

For each of the segmented images at low and high *Ca*, we identified and labeled each unique oil cluster, as shown in Figure 12. Each cluster is given a different color. The largest cluster has been colored blue to help distinguish the connectivity. Clusters can either be connected to the inlet, the outlet, or both, or be completely surrounded by other phases (these we call trapped ganglia).

Table 1 lists the proportion of oil, brine, and intermittent phases and the fraction of the oil phase that connects from inlet to outlet, both including the intermittent phase and without it. When the fractional flow increases both at low and high *Ca*, the number of trapped oil ganglia increases and the volume proportion of the largest oil cluster to the whole oil volume decreases. At low *Ca* we see a rapid drop in connectivity at the end of imbibition and all the oil phase is trapped.

For the lower *Ca*, the behavior is consistent with the traditional Darcy model of multiphase displacement, where at steady state flow occurs through stable, connected subnetworks of each phase in the pore space (Blunt, 2017). For the higher *Ca*, the behavior is different: ignoring the intermittent phase, the oil is only connected at the highest saturations and yet can flow and continues to be displaced as the water fractional flow increases. Hence, connectivity allowing movement and displacement of the oil phase is only provided by the periodic occupancy of some of the pore space, as seen during fast imaging (Reynolds et al., 2017). However, in the work of Reynolds et al. (2017) fluctuations in pore occupancy and connectivity were observed even at the lowest flow rates or a *Ca* of 1.4×10^{-7} using the definition in this paper: there are four possible reasons why this is not seen here. First, we

Figure 12. Three-dimensional images of oil clusters at different fractional flows when *Ca* is 3.0×10^{-7} and 7.5×10^{-6}: the macroscopic capillary numbers, equation (1), are 0.05 and 1.3, respectively. Each cluster is given a different color. Blue shows the largest oil cluster. The second column shows oil clusters at low *Ca*. The third column shows clusters of the oil and intermittent phases combined at high *Ca*, and the fourth column shows clusters of just the oil, excluding the intermittent phase. The number in the second and the fourth columns is the nonwetting phase Euler characteristic, Eu_{nw}. The number in the third column is the Euler characteristic of stable oil and intermittent phases combined.

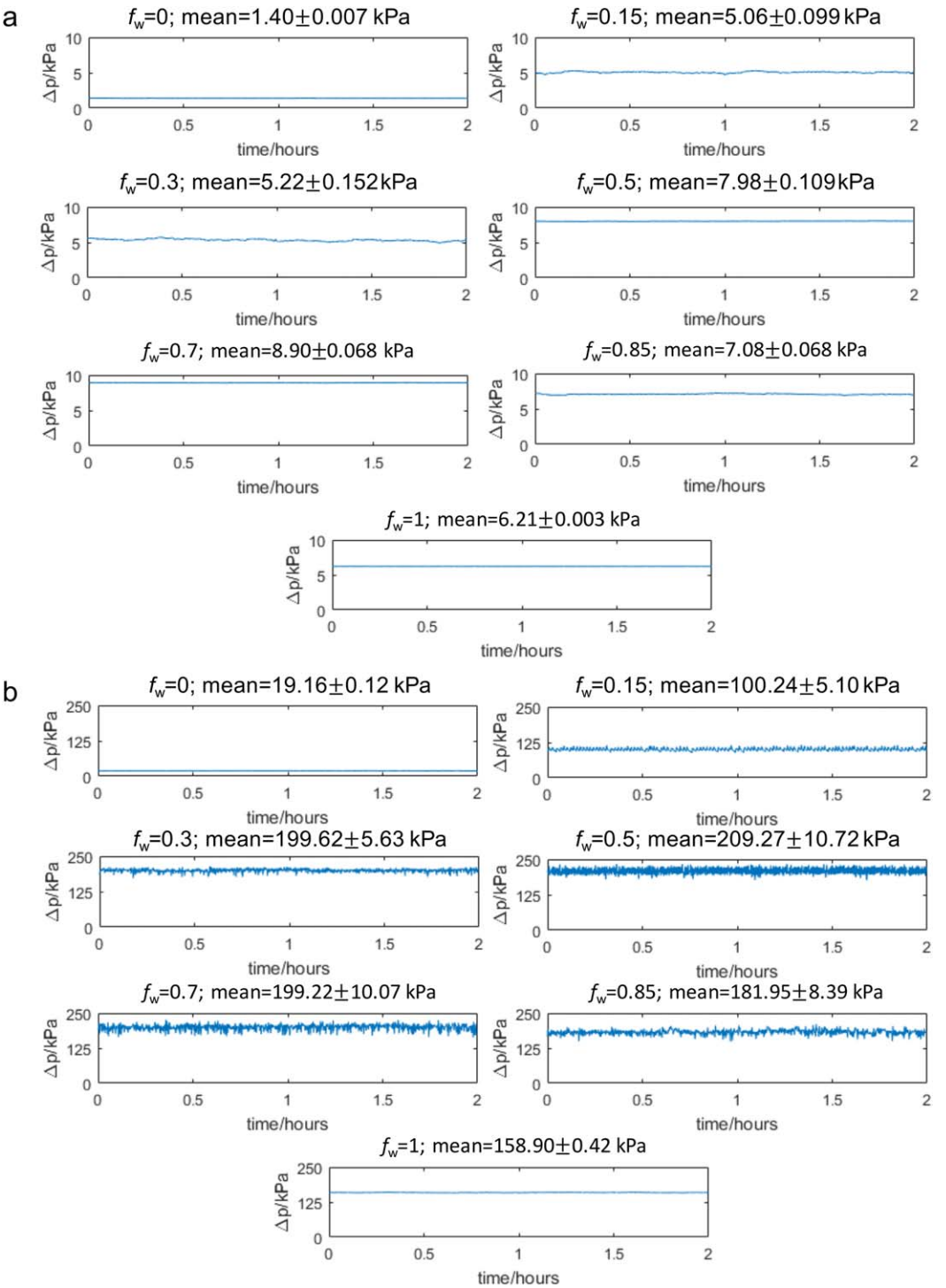


Figure 13. (a) Pressure difference measured between the inlet and outlet of the samples at low *Ca*. (b) Pressure difference measured between the inlet and outlet of the samples at high *Ca*. The mean pressure drop and standard deviation at each fractional flow are shown.

consider a two-fluid system with a high nonwetting phase viscosity which may suppress pore-scale interfacial fluctuations, as opposed to the nitrogen-brine system studied by Reynolds et al. (2017). Second, Reynolds et al. (2017) considered only one fractional flow during drainage where the nitrogen saturation was close to its percolation threshold, making disconnection possible with only a few displacement events.

Table 2
Saturation and Relative Permeability Calculated at Low and High Ca Over a Range of f_w

	$Ca = 3.0 \times 10^{-7}$			$Ca = 7.5 \times 10^{-6}$		
f_w	S_w	k_{ro}	k_{rw}	S_w	k_{ro}	k_{rw}
0	0.252	0.310	0.000	0.145	0.567	0.000
0.15	0.463	0.073	0.013	0.528	0.092	0.015
0.3	0.491	0.058	0.025	0.552	0.038	0.016
0.5	0.517	0.027	0.027	0.560	0.026	0.025
0.7	0.536	0.015	0.034	0.592	0.016	0.037
0.85	0.589	0.009	0.051	0.622	0.009	0.050
1	0.642	0.000	0.069	0.663	0.000	0.067

Third, Reynolds (2017) injected the fluids for about 1 h before scanning, whereas our work indicates that a longer time is needed to reach steady state. Finally, in our experiments, we may be unable to distinguish regions of the void space where either water or oil only resides a small fraction of the time. Even accounting for the intermittent phase, we appear to have no connectivity for a fractional flow of 0.85 in the high *Ca* experiment, which does suggest that we do not capture some pores that oil only occupies fleetingly.

The Euler characteristic is also computed to indicate the connectivity of the nonwetting phase (Armstrong et al., 2016; Herring et al., 2013; Liu et al., 2017), and was calculated using the image analysis Avizo software. A large negative value indicates that the oil is well connected. A positive value indicates poor connectivity, with more isolated clusters than redundant loops in the structure. As shown in Figure 12, the nonwetting phase Euler characteristic was calculated at each fractional flow at each *Ca* (the second and fourth columns). In the third column, the Euler characteristic number is calculated by considering the oil and intermittent phases combined as the nonwetting phase. The Euler characteristic number increases with f_w, starting from a negative value and becoming positive, which shows that the nonwetting phase connectivity becomes lower as it is displaced by water. Even if we combine the intermittent and stable phase, the Euler characteristic is positive for all but the lowest water fractional flows. This indicates a poor connectivity of oil phase at high flow rates, with many isolated clusters. Again, the misidentification of some regions of the pore space occupied by one phase for a short time may lead us to underestimate the connectivity, since, as stated above, the oil continues to flow and is displaced.

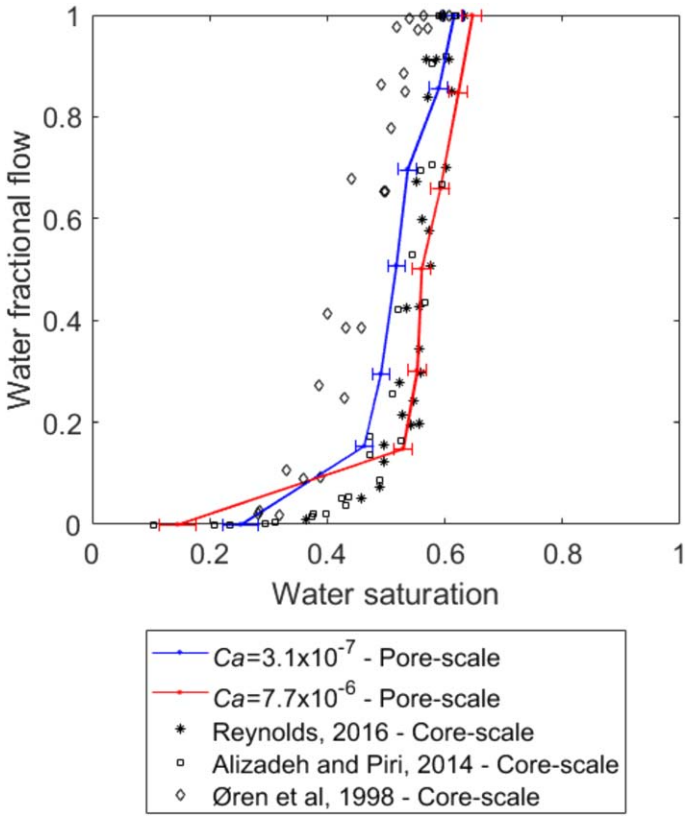


Figure 14. Fractional flow curves calculated at steady state for water-oil imbibition at low and high capillary number, $f_w(S_w)$ shown by the blue and red lines, respectively. The results are compared to five sets of cm-scale experimental data by Reynolds (2017), three sets of cm-scale experimental data by Alizadeh and Piri (2014), and three sets of cm-scale experimental data by Øren et al. (1998). Error bars in the *x*-direction consider uncertainties in the measured saturation caused by the threshold value chosen during image segmentation.

3.5. Relative Permeability

The pressure difference between the inlet and outlet of the core holder was measured using the pressure differential transducer shown in Figure 1. This was performed at steady state conditions which were identified by observing a constant average saturation across the scanned volume (Figure 11) and a stable, constant pressure drop. In this experiment, we recorded the pressure drop during the last 2 h of the total 10–20 h during which a constant fractional flow was imposed. The scans were taken during the final hour. Figure 13 demonstrates the pressure drop at each fractional flow and the corresponding mean value and standard deviation during the final 2 h: in all cases, the results imply steady state while the core was scanned: we have corrected for the additional pressure drop in the flow lines, see section 2.2.

For $f_w = 0$ and 1, and for low *Ca*, the pressure profile is smooth, which indicates an unchanging fluid configuration, consistent with the absence of an intermittent phase in these cases. However, for intermediate f_w and high *Ca*, the pressure does experience rapid fluctuations (Rücker et al., 2015a; Schlüter et al., 2017; Sinha et al., 2017). The hypothesis is that these represent local pore-scale displacement events, rather than being an artifact of the pump rates or noise in the transducers. A typical throat radius, *r*, for Bentheimer is 24 μm (Blunt, 2017); a representative capillary pressure for a piston-like event is $2\sigma/r$, or around 4 kPa in this case. At low *Ca*, the standard deviation in the pressure drop is much lower than this, meaning that the opportunity for fluid rearrangement is limited, whereas for higher *Ca*, the pressure fluctuations are sufficiently large to engender local displacement. The energy supplied from pumping fluids through the core is sufficient to allow a significant

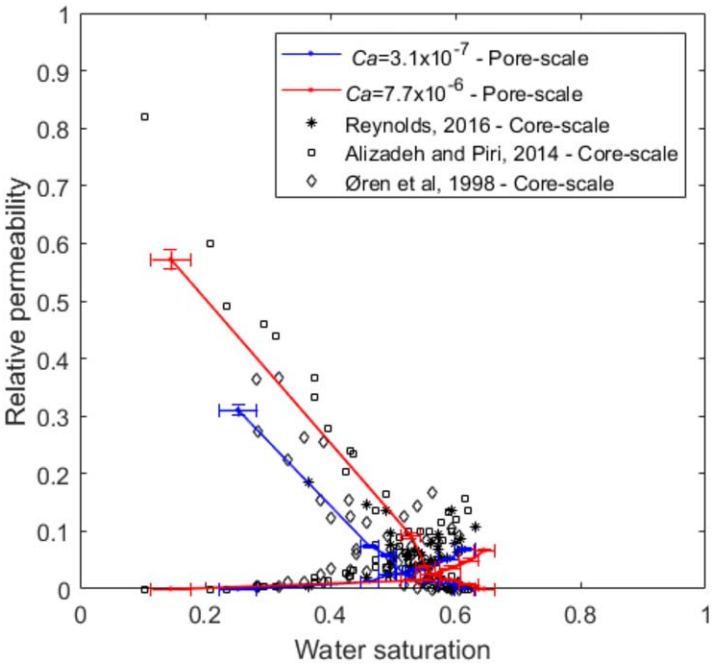


Figure 15. Relative permeabilities calculated at steady state for water-oil imbibition at low and high capillary numbers, *Ca*, shown by the blue and red lines, respectively. The results are compared to five sets of cm-scale experimental data by Reynolds (2017), three sets of cm-scale experimental data by Alizadeh and Piri (2014), and three sets of cm-scale experimental data by Øren et al. (1998). Error bars in the *y*-direction consider uncertainties in the measurement of the length and diameter of the sample, the absolute permeability, pressure measurements, and the pump rates. Error bars in the *x*-direction consider uncertainties in the measured saturation caused by the threshold value chosen during image segmentation.

fraction of the pore space to experience displacement at the higher capillary number (Reynolds et al., 2017).

The absolute permeability measured using the same transducer is $2.045(\pm 0.056) \times 10^{-12}$ m^2. The relative permeability is calculated by:

$$k_{rw} = \frac{Q_w \mu_w L}{A \Delta p K}; k_{ro} = \frac{Q_o \mu_o L}{A \Delta p K} \quad (4)$$

where k_{rw} is the brine relative permeability, k_{ro} is the oil relative permeability, Q_w is the brine flow rate (m^3/s), Q_o is the oil flow rate (m^3/s), μ_w is the brine viscosity (Pa s), μ_o is the oil viscosity (Pa s), L is the length of the whole sample (m), A is the cross area of the sample (m^2), k is the absolute permeability (m^2), and Δp is the pressure difference across the sample (Pa).

Table 2 lists the wetting phase saturation with the measured oil and brine relative permeabilities at each fractional flow for low and high capillary numbers. Note that the saturation values are estimated from only the scanned region of the core, while the pressure drops are measured across the whole sample. Figure 14 shows the estimated fractional flow curves at steady state for water-oil imbibition at low and high capillary numbers. Figure 15 shows the relative permeabilities plotted as functions of wetting phase saturation. At the lower *Ca*, the initial water saturation at the end of primary drainage was 0.252 $\pm$ 0.030 and the residual oil saturation at the end of imbibition was 0.358 $\pm$ 0.005. The errors are estimated from the root-mean square uncertainties in phase volume, total volume, and porosity during image segmentation. At the higher *Ca*, the initial water saturation and residual oil saturation were 0.145 $\pm$ 0.031 and 0.337 $\pm$ 0.003, respectively. Note that at the higher flow rate we see finite relative permeabilities even where regions of the pore space always occupied by oil (for a given fractional flow) do not connect from inlet to outlet. The only way that the oil can be displaced is through the intermittent filling of some pores allowing portions of the oil to be connected and flow.

The relative permeability data and the fractional flow, $f_w(S_w)$, obtained by our experiment at the mm-scale are compared with the data collected from experiments which were conducted at the core scale, as shown in Table 3.

In this paper, we are employing cores that are smaller than those used in conventional analysis. Our results are only valid if our sample size exceeds the representative elementary volume. Arns et al. (2003) demonstrated numerically that cubes of size 1 mm^3 or more are sufficiently large to estimate permeability for the Bentheimer sandstone used in this study. Hilfer and Lemmer (2015) found that for Fontainebleau sandstone, the representative elementary volume is around 3 mm (a volume of 27 mm^3) for porosity and around 250 mm^3 for permeability. Bentheimer is a homogeneous sandstone with a grain size from 0.1 to 0.38 mm (Reynolds & Krevor, 2015), which is similar to Fontainebleau sandstone which has a grain size from 0.1 to 0.4 mm (Delfosse-Ribay et al., 2004). For saturation, our imaging volume is 68 mm^3, while the total sample volume (used for the pressure measurements) is 1,180 mm^3; this latter volume is above the representative elementary volume calculated by Hilfer and Lemmer (2015), while the constancy of average saturation within the imaging volume (Figure 12) indicates that this is also accurately estimated.

As Figure 15 shows, our data are within the range of larger-scale experiments, with the low *Ca* results closer to the low *Ca* experiments

Table 3
Comparison of Ca and Sample Size Between This Work and Published Work

Author	Fluid system	Diameter (mm)	Length (mm)	*Ca*
This work	Oil-water	4.99 $\pm$ 0.01	60 $\pm$ 0.01	3.0×10^{-7}; 7.5×10^{-6}
Reynolds (2017)	CO_2-water; N_2-water	38	239	$2.6 - 8.0 \times 10^{-6}$
Alizadeh and Piri (2014)	Oil-water; gas-water; gas-oil	38.1	152.4	$2 - 3 \times 10^{-7}$
Øren et al. (1998)	Oil-water			1.7×10^{-6}

of Alizadeh and Piri (2014) and the high *Ca* results closer to the higher *Ca* experiments of Reynolds (2017). In this case, for a homogeneous sandstone, we suggest that we are able, simultaneously, to assess pore-scale occupancy and measure macroscopic properties, such as saturation and relative permeability, reliably.

4. Conclusions

We have developed an X-ray tomography-based experimental and image analysis methodology to measure the relative permeability and associated pore occupancy. We have performed imbibition using oil-brine and measured steady state relative permeability on a sandstone rock core at a low and high capillary number, *Ca*: 3.0×10^{-7} and 7.5×10^{-6}. During the hour-long scan time, it appeared that there were regions of the pore space that were occupied alternately by oil and brine. This intermittent phase was identified by obtaining the differential image between a doped brine image and the scans taken at each fixed fractional flow. The pressure drops at each fractional flow at low and high *Ca* were measured by high-precision pressure differential sensors and used to calculate the relative permeability.

We show that at the lower *Ca*, the oil and water phase occupancy appears to be constant with flow provided by fixed connected subnetworks through the pore space, consistent with conventional theory. At the higher *Ca*, we see that a significant fraction of the pore space is occupied by this intermittent phase, interpreted as regions of the void space where, during the scan, oil and water are both present. The oil phase in regions where it is always present is not connected, and yet it continues to flow and is displaced when the water fractional flow increases. The intermittent regions of the pore space are therefore necessary to allow the oil to flow, even if the connectivity is only periodically present.

The measured relative permeabilities compare well with literature measurements on larger cm-scale cores. Furthermore, our method potentially is faster, as it takes less time to achieve steady state in a smaller core, while providing pore-scale information on fluid configurations.

In future work, we could repeat these experiments, but at a synchrotron imaging facility with faster scan times to confirm, directly, this intermittent or dynamic connectivity, as seen already for brine-nitrogen flow (Reynolds et al., 2017). The relative permeability could also be computed from the measured pore-scale configurations of fluid and compared to the experimental measurements (Armstrong et al., 2016). In addition, the technique could be applied to a wide range of rock types and wettabilities. Lastly, the quantitative analysis of pore occupancy could be used for validation or input into simulation studies to explain and predict the observed displacement behavior.

Acknowledgments
We gratefully acknowledge funding from the Qatar Carbonates and Carbon Storage Research Centre (QCCSRC), provided jointly by Qatar Petroleum, Shell, and the Qatar Science & Technology Park. The images acquired in this study can be downloaded from https://doi.org/10.6084/m9.figshare.5607730.

References

Alizadeh, A. H., & Piri, M. (2014). The effect of saturation history on three-phase relative permeability: An experimental study. *Water Resources Research*, *50*, 1636–1664. https://doi.org/10.1002/2013WR014914

Al-Khulaifi, Y., Lin, Q., Blunt, M. J., & Bijeljic, B. (2017). Reaction rates in chemically heterogeneous rock: Coupled impact of structure and flow properties studied by X-ray microtomography. *Environmental Science & Technology*, *51*, 4108–4116. https://doi.org/10.1021/acs.est.6b06224

Andreas, J. M., Hauser, E. A., & Tucker, W. B. (1938). Boundary tension by pendant drops 1. *Journal of Physical Chemistry*, *42*, 1001–1019.

Andrew, M., Bijeljic, B., & Blunt, M. J. (2013). Pore-scale imaging of geological carbon dioxide storage under in situ conditions. *Geophysical Research Letters*, *40*, 3915–3918. https://doi.org/10.1002/grl.50771

Andrew, M., Menke, H., Blunt, M. J., & Bijeljic, B. (2015). The imaging of dynamic multiphase fluid flow using synchrotron-based x-ray microtomography at reservoir conditions. *Transport in Porous Media*, *110*, 1–24.

Armstrong, R. T., Georgiadis, A., Ott, H., Klemin, D., & Berg, S. (2014). Critical capillary number: Desaturation studied with fast X-ray computed microtomography. *Geophysical Research Letters*, *41*, 55–60. https://doi.org/10.1002/2013GL058075

Armstrong, R. T., McClure, J. E., Berrill, M. A., Rücker, M., Schlüter, S., & Berg, S. (2016). Beyond Darcy's law: The role of phase topology and ganglion dynamics for two-fluid flow. *Physical Review E*, *94*, 43113. https://doi.org/10.1103/PhysRevE.94.043113

Arns, J.-Y., Arns, C. H., Sheppard, A. P., Sok, R. M., Knackstedt, M. A., & Val Pinczewski, W. (2003). Relative permeability from tomographic images: Effect of correlated heterogeneity. *Journal of Petroleum Science and Engineering*, *39*, 247–259. https://doi.org/10.1016/S0920-4105(03)00066-4

Avraam, D. G., & Payatakes, A. C. (1996). Flow regimes and relative permeabilities during steady-state two-phase flow in porous media. *International Journal of Multiphase Flow*, *22*, 127.

Bachu, S. (2003). Screening and ranking of sedimentary basins for sequestration of CO_2 in geological media in response to climate change. *Environmental Geology*, *44*, 277–289. https://doi.org/10.1007/s00254-003-0762-9

Berg, S., Armstrong, R., Ott, H., Georgiadis, A., Klapp, S. A., Schwing, A., . . . Stampanoni, M. (2014). Multiphase flow in porous rock imaged under dynamic flow conditions with fast X-ray computed microtomography. *Petrophysics*, *55*(4), 304–312.

Berg, S., Rücker, M., Ott, H., Georgiadis, A., van der Linde, H., Enzmann, F., . . . Wiegmann, A. (2016). Connected pathway relative permeability from pore-scale imaging of imbibition. *Advances in Water Resources*, *90*, 24–35. https://doi.org/10.1016/j.advwatres.2016.01.010

Blunt, M. J. (2017). *Multiphase flow in permeable media: A pore-scale perspective*. Cambridge, UK: Cambridge University Press.

Blunt, M. J., Bijeljic, B., Dong, H., Gharbi, O., Iglauer, S., Mostaghimi, P., . . . Pentland, C. (2013). Pore-scale imaging and modelling. *Advances in Water Resources*, *51*, 197–216. https://doi.org/10.1016/j.advwatres.2012.03.003

Buades, A., Coll, B., & Morel, J. M. (2005). A non-local algorithm for image denoising. In *IEEE computer society conference on computer vision and pattern recognition (CVPR 2005)*. San Diego, CA: IEEE. https://doi.org/10.1109/CVPR.2005.38

Buades, A., Coll, B., & Morel, J.-M. (2008). Nonlocal image and movie denoising. *International Journal of Computer Vision*, *76*, 123–139. https://doi.org/10.1007/s11263-007-0052-1

Burger, W., & Burge, M. J. (2016). *Digital image processing: An algorithmic introduction using Java*. London, UK: Springer.

Chatenever, A., & Calhoun, J. C. Jr. (1952). Visual examinations of fluid behavior in porous media—Part I. *Journal of Petroleum Technology*, *4*(6), 8. https://doi.org/10.2118/135-G

Datta, S. S., Dupin, J.-B., & Weitz, D. A. (2014a). Fluid breakup during simultaneous two-phase flow through a three-dimensional porous medium. *Physics of Fluids*, *26*, 62004. https://doi.org/10.1063/1.4884955

Datta, S. S., Ramakrishnan, T. S., & Weitz, D. A. (2014b). Mobilization of a trapped non-wetting fluid from a three-dimensional porous medium. *Physics of Fluids*, *26*, 22002.

Delfosse-Ribay, E., Djeran-Maigre, I., Cabrillac, R., & Gouvenot, D. (2004). Shear modulus and damping ratio of grouted sand. *Soil Dynamics and Earthquake Engineering*, *24*, 461–471. https://doi.org/10.1016/j.soildyn.2004.02.004

Georgiadis, A., Berg, S., Makurat, A., Maitland, G., & Ott, H. (2013). Pore-scale micro-computed-tomography imaging: Nonwetting-phase cluster-size distribution during drainage and imbibition. *Physical Review E*, *88*, 33002. https://doi.org/10.1103/PhysRevE.88.033002

Herring, A. L., Harper, E. J., Andersson, L., Sheppard, A., Bay, B. K., & Wildenschild, D. (2013). Effect of fluid topology on residual nonwetting phase trapping: Implications for geologic CO_2 sequestration. *Advances in Water Resources*, *62*, 47–58. https://doi.org/10.1016/j.advwatres.2013.09.015

Hilfer, R., & Lemmer, A. (2015). Differential porosimetry and permeametry for random porous media. *Physical Review E*, *92*, 13305. https://doi.org/10.1103/PhysRevE.92.013305

Hilfer, R., & Øren, P. E. (1996). Dimensional analysis of pore scale and field scale immiscible displacement. *Transport in Porous Media*, *22*, 53–72. https://doi.org/10.1007/BF00974311

Lin, Q., Al-Khulaifi, Y., Blunt, M. J., & Bijeljic, B. (2016). Quantification of sub-resolution porosity in carbonate rocks by applying high-salinity contrast brine using X-ray microtomography differential imaging. *Advances in Water Resources*, *96*, 306–322. https://doi.org/10.1016/j.advwatres.2016.08.002

Lin, Q., Bijeljic, B., Rieke, H., & Blunt, M. J. (2017). Visualization and quantification of capillary drainage in pore space of laminated sandstone by a porous plate method using differential imaging X-ray micro-tomography. *Water Resources Research*, *53*, 7457–7468. https://doi.org/10.1002/2017WR021083

Liu, Z., Herring, A., Arns, C., Berg, S., & Armstrong, R. T. (2017). Pore-scale characterization of two-phase flow using integral geometry. *Transport in Porous Media*, *118*, 99–117. https://doi.org/10.1007/s11242-017-0849-5

Menke, H. P., Andrew, M. G., Blunt, M. J., & Bijeljic, B. (2016). Reservoir condition imaging of reactive transport in heterogeneous carbonates using fast synchrotron tomography—Effect of initial pore structure and flow conditions. *Chemical Geology*, *428*, 15–26. https://doi.org/10.1016/j.chemgeo.2016.02.030

Morrow, N., & Buckley, J. (2011). Improved oil recovery by low-salinity waterflooding. *JPT Journal of Petroleum Technology*, *63*, 106–112.

Øren, P.-E., Bakke, S., & Arntzen, O. J. (1998). Extending predictive capabilities to network models. *SPE Journal*, *3*(4), 324–336. https://doi.org/10.2118/52052-PA

Pak, T., Butler, I. B., Geiger, S., van Dijke, M. I. J., & Sorbie, K. S. (2015). Droplet fragmentation: 3D imaging of a previously unidentified pore-scale process during multiphase flow in porous media. *Proceedings of the National Academy of Sciences of the United States of America*, *112*, 1947–1952. https://doi.org/10.1073/pnas.1420202112

Parker, J. C. (1989). Multiphase flow and transport in porous media. *Reviews of Geophysics*, *27*, 311–328. https://doi.org/10.1029/RG027i003p00311

Payatakes, A. C. (1982). Dynamics of oil ganglia during immiscible displacement in water-wet porous media. *Annual Review of Fluid Mechanics*, *14*, 365–393.

Reynolds, C. A. (2017). *Two-phase flow behaviour and relative permeability between CO_2 and brine in sandstones at the pore and core scales* (Doctor thesis). UK: Imperial College London.

Reynolds, C. A., & Krevor, S. (2015). Characterizing flow behavior for gas injection: Relative permeability of CO_2-brine and N_2-water in heterogeneous rocks. *Water Resources Research*, *51*, 9464–9489. https://doi.org/10.1002/2015WR018046

Reynolds, C. A., Menke, H., Andrew, M., Blunt, M. J., & Krevor, S. (2017). Dynamic fluid connectivity during steady-state multiphase flow in a sandstone. *Proceedings of the National Academy of Sciences of the United States of America*, *114*(31), 8187–8192.

Rücker, M., Berg, S., Armstrong, R., Georgiadis, A., Ott, H., Simon, L., . . . Kersten, M. (2015a). The fate of oil clusters during fractional flow: Trajectories in the saturation-capillary number space. In *Conference: International symposium of the society of core analysts 2015* (Vol. 7). Canada: St. John's Newfoundland and Labrador.

Rücker, M., Berg, S., Armstrong, R. T., Georgiadis, A., Ott, H., Schwing, A., . . . Kersten, M. (2015b). From connected pathway flow to ganglion dynamics. *Geophysical Research Letters*, *42*, 3888–3894. https://doi.org/10.1002/2015GL064007

Saif, T., Lin, Q., Bijeljic, B., & Blunt, M. J. (2017). Microstructural imaging and characterization of oil shale before and after pyrolysis. *Fuel*, *197*, 562–574. https://doi.org/10.1016/j.fuel.2017.02.030

Schlüter, S., Berg, S., Li, T., Vogel, H.-J., & Wildenschild, D. (2017). Time scales of relaxation dynamics during transient conditions in two-phase flow. *Water Resources Research*, *53*, 4709–4724. https://doi.org/10.1002/2016WR019815

Singh, K., Menke, H., Andrew, M., Lin, Q., Rau, C., Blunt, M. J., & Bijeljic, B. (2017). Dynamics of snap-off and pore-filling events during two-phase fluid flow in permeable media. *Scientific Reports*, *7*, 5192. https://doi.org/10.1038/s41598-017-05204-4

Sinha, S., Bender, A. T., Danczyk, M., Keepseagle, K., Prather, C. A., Bray, J. M., . . . Hansen, A. (2017). Effective rheology of two-phase flow in three-dimensional porous media: Experiment and simulation. *Transport in Porous Media*, *119*, 77–94. https://doi.org/10.1007/s11242-017-0874-4

Stauffer, C. E. (1965). The measurement of surface tension by the pendant drop technique. *Journal of Physical Chemistry*, *69*, 1933–1938.

Tallakstad, K. T., Knudsen, H. A., Ramstad, T., Løvoll, G., Maløy, K. J., Toussaint, R., & Flekkøy, E. G. (2009a). Steady-state two-phase flow in porous media: Statistics and transport properties. *Physical Review Letters*, *102*, 74502. https://doi.org/10.1103/PhysRevLett.102.074502

Tallakstad, K. T., Løvoll, G., Knudsen, H. A., Ramstad, T., Flekkøy, E. G., & Maløy, K. J. (2009b). Steady-state, simultaneous two-phase flow in porous media: An experimental study. *Physical Review E*, *80*, 36308. https://doi.org/10.1103/PhysRevE.80.036308

Wildenschild, D., & Sheppard, A. P. (2013). X-ray imaging and analysis techniques for quantifying pore-scale structure and processes in subsurface porous medium systems. *Advances in Water Resources*, *51*, 217–246. https://doi.org/10.1016/j.advwatres.2012.07.018